

11-2012

## Dynamic Electron Correlation Effects On The Ground State Potential Energy Surface Of A Retinal Chromophore Model

Samer Gozem

Mark Huntress


Igor Schapiro

Roland Lindh

Alexander A. Granovsky

*See next page for additional authors*

Follow this and additional works at: [https://scholarworks.bgsu.edu/chem\\_pub](https://scholarworks.bgsu.edu/chem_pub)

 Part of the [Chemistry Commons](#)

---

### Repository Citation

Gozem, Samer; Huntress, Mark; Schapiro, Igor; Lindh, Roland; Granovsky, Alexander A.; Angeli, Celestino; and Olivucci, Massimo, "Dynamic Electron Correlation Effects On The Ground State Potential Energy Surface Of A Retinal Chromophore Model" (2012). *Chemistry Faculty Publications*. 165.  
[https://scholarworks.bgsu.edu/chem\\_pub/165](https://scholarworks.bgsu.edu/chem_pub/165)

This Article is brought to you for free and open access by the Chemistry at ScholarWorks@BGSU. It has been accepted for inclusion in Chemistry Faculty Publications by an authorized administrator of ScholarWorks@BGSU.

---

**Author(s)**

Samer Gozem, Mark Huntress, Igor Schapiro, Roland Lindh, Alexander A. Granovsky, Celestino Angeli, and Massimo Olivucci

# Dynamic Electron Correlation Effects on the Ground State Potential Energy Surface of a Retinal Chromophore Model

Samer Gozem,<sup>†</sup> Mark Huntress,<sup>†</sup> Igor Schapiro,<sup>†,#</sup> Roland Lindh,<sup>‡</sup> Alexander A. Granovsky,<sup>§</sup> Celestino Angeli,<sup>||</sup> and Massimo Olivucci<sup>\*,†,⊥</sup>

<sup>†</sup>Department of Chemistry, Bowling Green State University, Bowling Green, Ohio 43403, United States

<sup>‡</sup>Department of Chemistry – Ångström, the Theoretical Chemistry Programme, POB 518, SE-751 20 Uppsala, Sweden

<sup>§</sup>Firefly Project, Moscow 117593, Russia

<sup>||</sup>Dipartimento di Chimica, Università di Ferrara, via Borsari 46, I-44121 Ferrara, Italy

<sup>⊥</sup>Dipartimento di Chimica, Università di Siena, via De Gasperi 2, I-53100 Siena, Italy

## Supporting Information

**ABSTRACT:** The ground state potential energy surface of the retinal chromophore of visual pigments (e.g., bovine rhodopsin) features a low-lying conical intersection surrounded by regions with variable charge-transfer and diradical electronic structures. This implies that dynamic electron correlation may have a large effect on the shape of the force fields driving its reactivity. To investigate this effect, we focus on mapping the potential energy for three paths located along the ground state CASSCF potential energy surface of the penta-2,4-dieniminium cation taken as a minimal model of the retinal chromophore. The first path spans the bond length alternation coordinate and intercepts a conical intersection point. The other two are minimum energy paths along two distinct but kinetically competitive thermal isomerization coordinates. We show that the effect of introducing the missing dynamic electron correlation variationally (with MRCISD) and perturbatively (with the CASPT2, NEVPT2, and XMCQDPT2 methods) leads, invariably, to a stabilization of the regions with charge transfer character and to a significant reshaping of the reference CASSCF potential energy surface and suggesting a change in the dominating isomerization mechanism. The possible impact of such a correction on the photoisomerization of the retinal chromophore is discussed.

## INTRODUCTION

The penta-2,4-dieniminium cation (PSB3) is a conjugated and protonated imine which has been used extensively as a low-cost computational model of the retinal protonated Schiff base chromophore (rPSB) of visual pigments<sup>1–7</sup> (see Scheme 1). Indeed, PSB3 reproduces several features of 4-*cis*-nona-2,4,6,8-tetraeniminium cation (PSB5),<sup>8,9</sup> a model system that incorporates the five conjugating double bonds of native rPSB (since the sixth double bond residing on the  $\beta$ -ionone ring has a reduced conjugation<sup>10</sup>).

As illustrated in Scheme 1, at the complete-active-space-self-consistent-field (CASSCF) level of theory, the first singlet excited state ( $S_1$ ) surface of *cis*-PSB3 is characterized by a barrierless relaxation path connecting the Franck–Condon (FC) region to a peaked conical intersection (CI)<sup>1,11</sup> with the ground state ( $S_0$ ) energy surface. The CI structure is highly twisted about the central C2=C3 double bond and mediates the photochemical isomerization of *cis*-PSB3 to *trans*-PSB3.<sup>11</sup> The lowest energy CI<sup>12</sup> displays a geometry with a ca. 90° twisted central bond and a decreased bond length alternation (BLA) with respect to the  $S_0$  equilibrium structures (energy minima) *cis*-PSB3 and *trans*-PSB3.<sup>3,13</sup> The same scheme shows that, after decay in the CI region, the system must relax along the  $S_0$  potential energy surface. In spite of the fact that an exact knowledge of the properties of this surface is mandatory for the understanding of the relaxation process, little work has been devoted to its study. The main target of the present contribution is to address this issue.

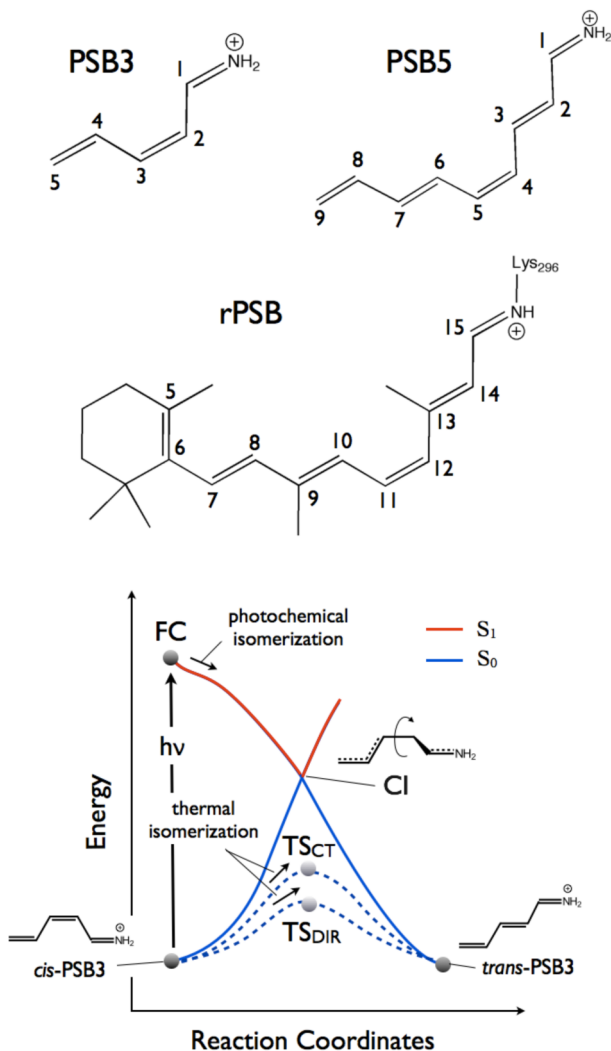
The CASSCF  $S_0$  potential energy surface of PSB3 is characterized, similar to PSB5,<sup>8,9</sup> by two transition states (see  $TS_{CT}$  and  $TS_{DIR}$  in Scheme 1) featuring a ca. 90° twisted central bond but opposite BLA patterns and both connecting *cis*-PSB3 to *trans*-PSB3. Therefore, both  $TS_{CT}$  and  $TS_{DIR}$  mediate the thermal isomerization of *cis*-PSB3 to *trans*-PSB3. Comparison of the optimized CI, *cis*-PSB3, *trans*-PSB3,  $TS_{CT}$ , and  $TS_{DIR}$  structures and relative CASSCF stabilities (see Scheme 2) supports the landscape depicted in Figure 1A. This represents a low-lying two-dimensional cross-section of the PSB3  $S_0$  CASSCF/6-31G\* potential energy surface spanning a reaction coordinate (RC) dominated by the twisting deformation about the C2=C3 double bond and a BLA coordinate dominated by an inversion between double and single bonds. As we will explain below, in the CI region, the coordinate space along RC and BLA is roughly parallel to the branching plane<sup>14</sup> associated with the CI.

Charge distribution analysis demonstrates that PSB3 (as well as PSB5) features a variable electronic structure along the  $S_0$  potential energy surface.<sup>8</sup> Indeed, as shown in Scheme 2 and Figure 1A, one of the transition states ( $TS_{DIR}$ ) displays a diradical character consistent with an  $S_0$  isomerization mechanism driven by the homolytic breaking of the central C2=C3 double-bond. Therefore,  $TS_{DIR}$  has two unpaired electrons located on the  $\pi$  systems of the nearly orthogonal allyl

Received: April 18, 2012

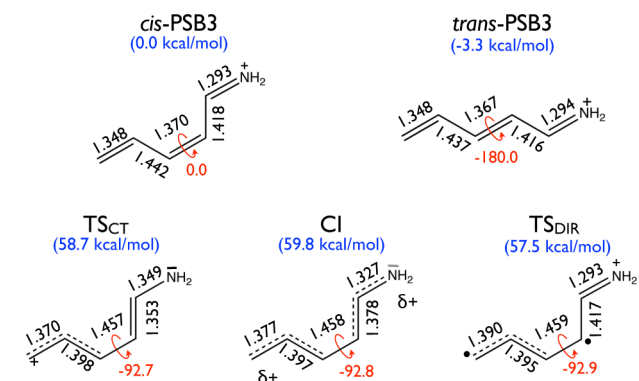
Published: September 6, 2012

Scheme 1. (Top) The Structures of the *cis*-Penta-2,4-dieniminium Cation (PSB3), the 4-*cis*-Nona-2,4,6,8-dieniminium Cation (PSB5), and the 11-*cis*-Retinal Protonated Schiff Base (rPSB) Which Is Connected to the Lys296 Residue in Bovine Rhodopsin and (Bottom) Schematic, One-Dimensional Representation of the Potential Energy Surfaces of PSB3



(C5H<sub>2</sub>-C4H-C3H-) and protonated imine heteroallyl (-C2H-C1H-NH<sub>2</sub>) moieties. In contrast, the other transition state (TS<sub>CT</sub>) displays a charge-transfer (closed-shell) character with an augmented electron density (and therefore a reduced positive charge) in the N=C1 region with respect to that of the *cis* and *trans* equilibrium geometries. The contrasting charge distributions of TS<sub>DIR</sub> and TS<sub>CT</sub> indicate the existence of two low-lying regions on the S<sub>0</sub> potential energy surface of protonated Schiff bases where qualitatively different  $\pi$ -electron densities are observed. One region encompasses most of the S<sub>0</sub> potential energy surface (including TS<sub>DIR</sub> and the *cis*-PSB3 and *trans*-PSB3 equilibrium structures) and is characterized by a wave function with a predominantly correlating covalent/diradical configuration ( $\psi_{\text{DIR}}$ ), while the other region is dominated by a charge-transfer (singly excited) configuration ( $\psi_{\text{CT}}$ ). Note that since we generally describe regions in the proximity of a CI, we chose to use the “DIR” label to describe the covalent wave function although the corresponding

Scheme 2. Main CASSCF/6-31G\* Geometrical Parameters (Bond Lengths in Ångstroms and C1-C2-C3-C4 Dihedrals in Degrees) and Relative Energies (Value in Parentheses in kcal/mol) for the S<sub>0</sub> Stationary Points and Conical Intersection of PSB3<sup>a</sup>



<sup>a</sup>The resonance formula also provides a qualitative representation of the singlet electron pairing and charge distribution. It is apparent that in TS<sub>CT</sub> there are no singlet paired electrons along C2-C3. Thus, the C2=C3 double bond will not be readily reconstituted upon planarization. This is not happening in TS<sub>DIR</sub> where one has two singlet spin paired radical centers ready to couple. The resonance formula used for the CI represents a mixture of the intersection TS<sub>CT</sub> and TS<sub>DIR</sub> electronic configurations.

electronic structure varies from closed shell at the reactant and product to diradical for twisted geometries due to homolytic cleavage of the central  $\pi$  bond.

Recently we reported the results of semiclassical trajectory computations for a CASSCF/6-31G\*/AMBER model of bovine rhodopsin (Rh), a dim-light rod visual pigment.<sup>15</sup> Such trajectories provided a simulation of the 11-*cis* to all-*trans* photochemical isomerization of rPSB in Rh. The analysis of the charge distribution along different trajectories indicated that upon S<sub>1</sub> to S<sub>0</sub> decay in the region of a CI (where the reactive C11=C12 double-bond is fully twisted), the rPSB chromophore may evolve along a charge-transfer region of the S<sub>0</sub> potential energy surface. A direct chemical consequence of such an event is that the double-bond reconstitution is delayed as  $\psi_{\text{CT}}$  imposes a single bond character along C11=C12. This has been demonstrated for PSB3 by a quantitative valence-bond analysis of the CASSCF wave function<sup>11</sup> showing that in  $\psi_{\text{DIR}}$  singlet spin-paired  $\pi$  electrons are ready to recouple along the reactive bond while in  $\psi_{\text{CT}}$  the  $\pi$  electrons are spin-paired along adjacent bonds. In other words, even if the chromophore starts twisting along the reaction (isomerization) coordinate, it will have to find its way to a region dominated by the  $\psi_{\text{DIR}}$  configuration before the  $\pi$ -bond reconstitution can begin. As detailed in ref 15, such a delay has an impact on the fate of the trajectory that may result in either a reactive (i.e., leading to the bathorhodopsin photoproduct) or nonreactive (i.e., leading back to the Rh reactant) event and, in principle, on the reaction quantum yield.

While the regions of the S<sub>0</sub> potential energy surface describing the transition between the charge-transfer and covalent states of PSB3 and Rh are presently unknown, the difference in the  $\pi$ -electron density associated with  $\psi_{\text{DIR}}$  and  $\psi_{\text{CT}}$  suggests that dynamic electron correlation would play a key role in determining their relative extension and stability.<sup>16,17</sup> Therefore, *dynamic electron correlation may significantly alter the shape of the reference CASSCF landscape*

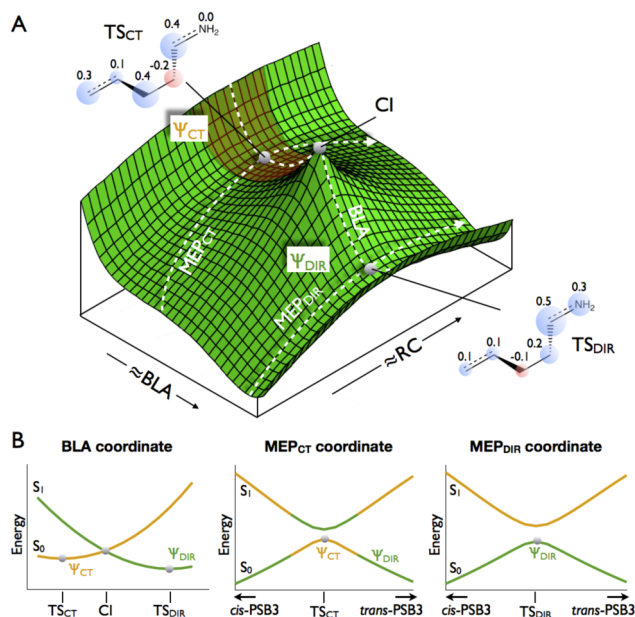


**Figure 1.** Low-lying ground state potential energy surface of PSB3. (A) Schematic two-dimensional cross-section of the  $S_0$  potential energy surface of PSB3. The two geometrical coordinates are dominated by bond length alternation (BLA) and the C2–C3 twisting reaction coordinate (RC), respectively. The surface region dominated by a charge-transfer wave function ( $\psi_{CT}$ ) is displayed in brown, while that dominated by a covalent/diradical wave function ( $\psi_{DIR}$ ) is displayed in green. The electronic structures of the two transition states are described with a bubble diagram representing the total Mulliken charge along the backbone of PSB3 (charges summed onto heavy atoms). The values of these charges are displayed. Finally, the three paths used in the present study (BLA coordinate,  $MEP_{CT}$ , and  $MEP_{DIR}$ ) are schematically represented as dashed lines on the surface. (B)  $S_0$  and  $S_1$  two-root SA-CASSCF/6-31G\* energy profiles along the three paths represented in part A. Brown regions correspond to regions dominated by a charge transfer wave function, while green regions are predominantly covalent (although the contribution of charge transfer character in these regions also varies).

of Figure 1A with potentially important chemical consequences. For instance, in a situation in which an ensemble of semiclassical trajectories is computed to simulate the population dynamics of Rh, an extended and more stable charge-transfer region may increase the percentage of trajectories traveling along that region and the average time spent in it after  $S_1$  to  $S_0$  decay. This is expected to dramatically change the  $S_0$  evolution of the initially excited population toward the product valley.

In a recent study, Mori et al.<sup>7</sup> investigated the effect of dynamic electron correlation on the geometry of the minimum energy CI in PSB3. Moreover, Valsson and Filippi<sup>6</sup> studied the effect of dynamic electron correlation on the  $S_1$  isomerization of PSB3, with special attention to the FC region and the minimum energy path connecting the FC to the CI. In the present study, we build on these two studies by investigating the effect of dynamic electron correlation on the shape and stability of the  $S_0$  potential energy surface surrounding the CI. Accordingly, we characterize the CASSCF/6-31G\* surface of the PSB3 along three potential energy paths (see Figure 1B). The first corresponds to a coordinate obtained via a linear interpolation (and extrapolation) of the optimized  $TS_{CT}$  and  $TS_{DIR}$  structures (BLA). This interpolation intercepts a single CI point that is located between the two transition structures (the structure of this CI intercepted by the BLA path is shown

in Scheme 2). The second ( $MEP_{DIR}$ ) corresponds to the minimum energy path connecting  $TS_{DIR}$  to the *cis* reactant and the *trans* product where the wave function remains predominantly covalent ( $\psi_{DIR}$ ). The third ( $MEP_{CT}$ ) corresponds, again, to a minimum energy path describing the isomerization coordinate passing through  $TS_{CT}$  and connecting reactant and product. However, this path intercepts regions dominated by different electronic configurations ( $\psi_{CT}$  or  $\psi_{DIR}$ ).

The results reported below show that incorporation of dynamic electron correlation on top of the CASSCF wave function using either variational (MRCISD) or perturbative (MRPT2) theories consistently leads to a stabilization of the region dominated by the charge-transfer configuration ( $\psi_{CT}$ ) with respect to the rest of the surface. Accordingly, the  $TS_{CT}$  structure becomes the lowest energy saddle point on the PSB3  $S_0$  potential energy surface. Consistently with the results of Mori et al.,<sup>7</sup> the same effect leads to a shift in the position and shape of the CI along the BLA coordinate and toward  $TS_{DIR}$ .

## METHODS

The dynamic electron correlation is introduced on top of the reference CASSCF wave function in a variational scheme using the MRCISD and MRCISD+Q methods and also using different implementations of multireference second order perturbation theory (MRPT2) such as single state CASPT2<sup>18</sup> (referred to hereafter as simply CASPT2), multistate-CASPT2 (MS-CASPT2),<sup>19</sup> XMCQDPT2,<sup>20</sup> and QD-NEVPT2.<sup>21–23</sup> We now revise the methods used for generating structures along the paths of Figure 1 and present details about the multireference methods used.

**Reference Potential Energy Surface.** CASSCF structures and energies were computed using the MOLCAS 7.6 quantum chemistry software package.<sup>24</sup>  $TS_{CT}$  and  $TS_{DIR}$  were both optimized at the equal-weight two-root state averaged (SA)-CASSCF/6-31G\* level. The basis set employs Cartesian d polarization functions. The active space comprises the six  $\pi$ -orbitals of PSB3 occupied with six electrons (6-in-6). The CASSCF wave functions were then used as zero-order approximations for the higher level methods described below. From the two transition state structures, the BLA path was produced by using a linear interpolation/extrapolation of their coordinates to give a set of 14 structures (including the two transition states) spanning the corresponding BLA coordinate. Throughout this work, we define the BLA coordinate as the difference between the average bond length (in Ångstroms) of formal double bonds (N=C1, C2=C3, and C4=C5) and formal single bonds (C1–C2 and C3–C4). The other two paths ( $MEP_{CT}$  and  $MEP_{DIR}$ ) were produced by running two IRC calculations for each path at the CASSCF level of theory with a step size of  $0.01 \text{ \AA} \cdot (\text{amu})^{1/2}$  and starting from the corresponding transition state. The resulting  $MEP_{CT}$  and  $MEP_{DIR}$  paths represent thermal isomerizations from *cis*-PSB3 to *trans*-PSB3. Since, in this study, we are mainly concerned with the region surrounding the CI, we do not consider the whole path, which comprises over 100 geometries, but rather only the eight structures closest to the transition states from each side (thus each path includes 17 geometries including the transition state). The CASSCF/6-31G\* energy profiles along the BLA,  $MEP_{CT}$ , and  $MEP_{DIR}$  paths are shown in Figure 1B. Unless otherwise specified, the CASSCF reference wave function and basis set are the same as the ones used for the geometry optimization.

In order to determine the relaxed structure and branching plane vectors characterizing the CI, the Gaussian '03 software package was used.<sup>25</sup> The CI structure shown in scheme 2 provided a guess initial structure for the CI optimization. A conical intersection optimization was performed with the two-root SA-CASSCF method and the reduced maximum step size of 0.05 Bohr, which converged to a solution in five iterations and provided the branching plane vectors corresponding to the CI geometry.

**Multireference Calculations.** Single point CASPT2 and MS-CASPT2 energies were computed using the MOLCAS 7.6 quantum chemistry software package.<sup>24</sup> For these calculations, an imaginary shift of 0.2 was used to exclude intruder states, consistent with previous studies. The effect of the ionization potential-electronic affinity (IPEA) shift on CASPT2 energies is considered. The IPEA parameter reduces a systematic error through a modification of the zeroth order Hamiltonian, and its 0.25 value has been obtained by fitting a specific set of experimental data<sup>26</sup> (see also the discussion in ref 27 for systems that require different IPEA values). CASPT2 energies reported with the IPEA shift are labeled with "IPEA=0.25;" otherwise the reported CASPT2 values and geometries are obtained with IPEA=0. The reported QD-NEVPT2 energies are based on the partially contracted variant of NEVPT2<sup>22</sup> using state-specific sets of canonical inactive and virtual orbitals as opposed to the same set of state average orbitals. XMCQDPT2 energies were computed using Firefly version 7.1.G, build number 5620.<sup>28</sup> For the XMCQDPT2 calculations, the intruder state avoidance (ISA) shift was set to 0.02 for avoiding the intruder states. MRCISD energies were computed using both the internally contracted (IC)<sup>29</sup> and uncontracted variants. IC-MRCISD energies were computed with the Molpro<sup>30</sup> package while uncontracted MRCISD energies were computed with the Columbus quantum chemistry software package.<sup>31–34</sup> The integrals for Columbus were obtained with the Dalton quantum chemistry software.<sup>35</sup> The full CASSCF active space (6-in-6) was included in the reference space for MRCISD and IC-MRCISD calculations. Generalized interacting space restriction was used for uncontracted MRCISD. The original Davidson correction (Q) was used for MRCISD+Q calculations (for the effect of using alternative corrections, see the Supporting Information, SI). The 1s core orbitals in carbon and nitrogen atoms were kept frozen for all multireference calculations, and in all cases the 6-31G\* basis set with Cartesian d polarization functions was consistently used. However, MRCISD+Q energy profiles along the BLA coordinate were also computed using the 3-21G, 6-31++G\*\*, and 6-311G\* basis sets to test the effect of the basis set quality on the relative energies of the states with  $\psi_{CT}$  and  $\psi_{DIR}$  character (see the SI). The effect of expanding the basis set was found to slightly stabilize charge transfer electronic characters.

In the present work, MRCISD and MRCISD+Q energy profiles are reported for the uncontracted variant. The IC-MRCISD and uncontracted MRCISD energy profiles are very similar (see the SI). However, MRCISD charge transfer profiles are computed for the IC-MRCISD variant with Molpro (population analysis in Columbus is incompatible with our use of a basis set with Cartesian d functions). All charges reported in this study are computed with the Mulliken population analysis. The charge-transfer and covalent/diradical characters (i.e., the weights of the  $\psi_{DIR}$  and  $\psi_{CT}$  configurations, respectively) are measured indirectly by computing the total

Mulliken charge of the allyl moiety (C5H<sub>2</sub>-C4H-C3H-) which is separated from the Schiff base moiety (-C2H-C1H-NH<sub>2</sub>) by the isomerizing C2=C3 bond. The XMCQDPT2 charges (computed in Firefly) and QD-NEVPT2 and MS-CASPT2 charges (computed externally) were derived from the wave functions obtained by the diagonalization of the effective Hamiltonian evaluated at the 0+1+2 order. These wave functions are linear combinations of the two SA-CASSCF wave functions, and thus they belong to the CAS space. The charges therefore include the most important effects caused by state mixing while omitting other contributions from the first-order interacting space.

In this study, we have invariably employed a two-root state averaging for the reference CASSCF wave functions. The consequences of this choice have been assessed (see the SI for a full analysis) by performing a series of state average computations with additional roots (the roots are always taken with equal weights) for the transition state TS<sub>CT</sub>. We found that the S<sub>0</sub>-S<sub>1</sub> energy gap is, in general, sensitive to the number of roots used in CASSCF and in most MRPT2 methods, and even in MRCISD. The changes are rationalized by considering that when a covalent root is added to the state average set, the weight of the states with the corresponding charge distribution is increased in the averaged molecular orbital description. This behavior explains the difference between our two-root results and the three-root results by Mori et al.<sup>7</sup> showing a displaced CI in PSB3 at the CASSCF level of theory. However, the MRCISD+Q level reduces the dependence, and the energies become less sensitive to the number of roots used in the generation of the reference wave function. It is shown that minimal state-averaging may be the best compromise in order to get more accurate CASSCF and MRPT2 energies. Better MRPT2 accuracies may be achieved by increasing the dimension (i.e., adding more CASCI states) in the construction of the effective Hamiltonian (e.g., in XMCQDPT2) while keeping the underlying state-averaging scheme for CASSCF the same, as shown in the case of butadiene in ref 20.

In the Results and Discussion, we also present the effect of optimizing the BLA, MEP<sub>CT</sub>, and MEP<sub>DIR</sub> paths with CASPT2 and XMCQDPT2, which are representative MRPT2 methods. Due to the unavailability of analytical gradients for these methods, numerical gradients were used (these methods are available in Molcas 7.6 for CASPT2 and in the developer's version of Firefly for XMCQDPT2). The *cis*-PSB3, *trans*-PSB3, TS<sub>CT</sub>, and TS<sub>DIR</sub> structures were reoptimized with the MRPT2 methods in a manner consistent with the CASSCF optimizations (also employing the same 6-31G\* basis set and number of roots). The BLA path was then generated by interpolation/extrapolation of the MRPT2 optimized TS<sub>CT</sub> and TS<sub>DIR</sub> structures, and the MEP<sub>CT</sub> and MEP<sub>DIR</sub> paths were generated using IRC calculations employing numerical gradients and started from the MRPT2 optimized transition states. CASPT2 IRC calculations used identical parameters to those performed with CASSCF since the same software package was employed for both calculations. XMCQDPT2 IRC calculations employed the Gonzalez-Schlegel second order method<sup>36</sup> and a stride of 0.0053 Å·(amu)<sup>1/2</sup>.

## RESULTS AND DISCUSSION

In the first three subsections, we systematically describe the changes in the shape of the PSB3 potential energy surface along the BLA, MEP<sub>CT</sub>, and MEP<sub>DIR</sub> coordinates following MRCISD

and MRPT2 computations using the common 6-31G\* basis. The effect of the geometrical relaxation of the surface stationary points at the MRPT2 level is investigated in the fourth subsection. A discussion of the quality of CASPT2//CASSCF/6-31G\* calculations widely used in photochemical and photobiological applications is given in the last subsection.

**BLA Path and Branching Plane.** The energy profiles along the BLA coordinate computed with CASSCF, MRCISD, MRCISD+Q, and various MRPT2 methods are shown in Figure 2A and B. We assume here that MRCISD+Q provides the quantitatively correct description of the different electronic

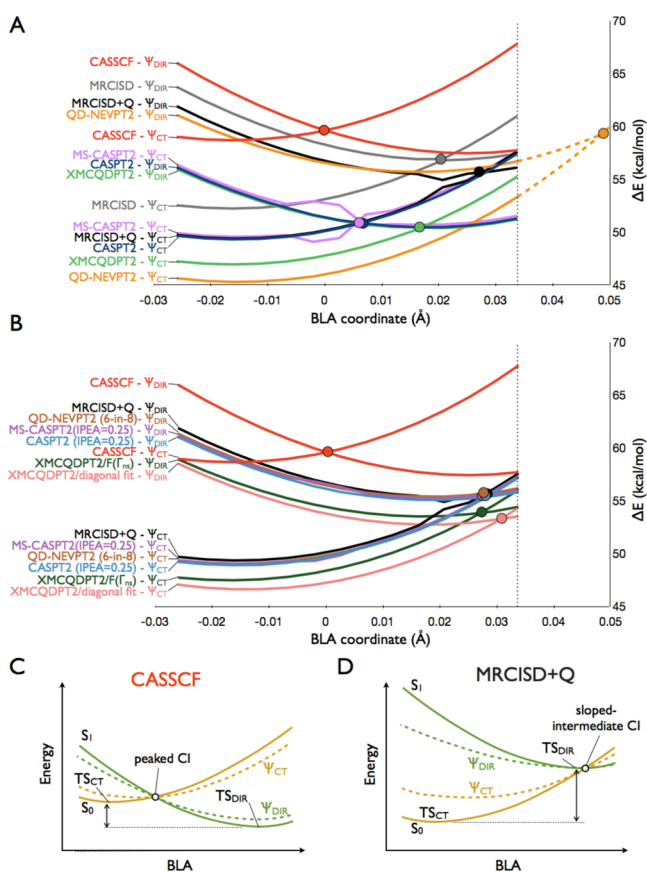


**Figure 2.** Energy profiles along the BLA coordinate compared with two-root SA-CASSCF (red) and MRCISD+Q (black) which are present in both parts A and B. The energy values are relative to the reactant (*cis*-PSB3). The position of the CI for each method is indicated with a filled circle. The curves are labeled at the left margin to distinguish between diabatic curves with predominantly charge transfer ( $\psi_{CT}$ ) and covalent-diradical ( $\psi_{DIR}$ ) character for each method. (A) The  $S_0$  and  $S_1$  energies for MRCISD (gray), CASPT2 (dark blue), MS-CASPT2 (magenta), QD-NEVPT2 (orange), and XMCQDPT2 (green). The QD-NEVPT2 CI does not lie within the selected BLA coordinate values, and so its position is estimated by extrapolating the QD-NEVPT2 curve using a polynomial fit (dashed line). (B) The  $S_0$  and  $S_1$  energies for CASPT2(IPEA=0.25) (blue), MS-CASPT2(IPEA=0.25) (violet), QD-NEVPT2 with 6-in-8 active space (brown), XMCQDPT2 with a diagonal fit (pink), and XMCQDPT2/ $F(\Gamma_{ns})$  (dark green). (C and D) Schematic valence bond-like state mixing diagrams for the  $S_0$  and  $S_1$  energy profiles along the BLA coordinate at the CASSCF and MRCISD+Q levels of theory, respectively. The diabatic states are represented with dashed lines. Mixing of the diabatic states produces the adiabatic states represented with solid lines. Brown curves are dominated by a charge transfer wave function, while green curves are dominated by a covalent one.

structures of PSB3. It is apparent that the selected reference CASSCF method not only overestimates energy barriers of the two transition states with respect to MRCISD+Q but displays a reverse stability order of  $TS_{CT}$  and  $TS_{DIR}$ . A discussion on the effect of dynamic electron correlation on the topology of the ground state is presented at the end of this section.

Consistent with the MRCISD+Q result, all MRPT2 methods seem to yield the same change characterized by the  $TS_{CT}$  stabilization and the CI shifting toward  $TS_{DIR}$ . On the other hand, the magnitude of the charge-transfer stabilization depends on the method. CASPT2 and MS-CASPT2 yield the same energy profile for the charge-transfer state as MRCISD+Q but, as expected,<sup>26</sup> an overstabilized covalent curve due to the lack of IPEA shift. In Figure 2B, we show that the incorporation of the IPEA shift yields CASPT2(IPEA=0.25) and MS-CASPT2(IPEA=0.25) profiles substantially identical to MRCISD+Q. Our findings are consistent with a study on diatomic molecules where it was also found that CASPT2 with a modified zeroth-order Hamiltonian performs better than unmodified CASPT2 when compared to FCI.<sup>37</sup> XMCQDPT2 (Figure 2A) yields curves similar to MRCISD but both shifted to lower energies, and with a slightly overstabilized covalent curve with respect to MRCISD+Q. In Figure 2B, we report XMCQDPT2 results obtained using slightly different definitions of the model Fock-like operator used to define the zero-order Hamiltonian within the XMCQDPT2 formalism. Those modifications of the “classical” XMCQDPT2, termed “XMCQDPT2/diagonal fit” and “XMCQDPT2/ $F(\Gamma_{ns})$ ”, provide a more balanced description of states of very different nature and therefore produce energy profiles which are in better agreement with MRCISD+Q. More details about these methods are provided in the SI. Finally, the QD-NEVPT2 method leads to an overstabilization of the  $\psi_{CT}$  configuration with respect to MRCISD+Q. In contrast, the covalent curve is substantially on top of MRCISD+Q. For this reason, when using the reference CASSCF wave function defined above, QD-NEVPT2 yields a considerably shifted position of the CI. The QD-NEVPT2 CI is shown in an extrapolation of the path in Figure 2A. This overstabilization of the charge transfer configuration is due to the limit in the zero-order CASSCF wave function and may be resolved by using a larger active space.<sup>38</sup> In fact, we find that the expansion of the active space to 6-in-8 allows the QD-NEVPT2 energy profile to virtually overlap with that of MRCISD+Q(6-in-6) (Figure 2B). Upon a similar active space expansion, CASPT2, CASPT2(IPEA=0.25), and XMCQDPT2 show a modest variation where their agreement with MRCISD+Q(6-in-6) decreases, as discussed in the SI.

In Figure 2A, we find an artifact along the MRCISD+Q profile (near 0.025 Å of the BLA coordinate) in correspondence with the MRCISD CI. This artifact is significantly reduced when using a Davidson correction with a relaxed or rotated reference, as discussed in ref 39 (also see the SI). A second, more pronounced artifact occurs along the MS-CASPT2 profile. This artifact is located in the vicinity of 0.00 Å along the BLA coordinate and therefore in correspondence with the CASSCF CI. Such behavior has been shown to arise in both CASPT2 and MS-CASPT2 if the corresponding CASSCF  $S_0$  and  $S_1$  wave functions (which in this case correspond to the  $\psi_{DIR}$  and  $\psi_{CT}$  configurations) are highly mixed, e.g., near a CI.<sup>20,40</sup> Solutions to this problem have already been proposed, and XMCQDPT2 does not suffer from this problem while QD-NEVPT2 reduces it. The XMCQDPT2 extension has recently

also been used for the development of the XMS-CASPT2 method.<sup>41</sup> However, here we are interested in the qualitative changes on wide regions of the potential energy surfaces, while these artifacts are localized. See the SI for a more detailed discussion of those artifacts.

It is of interest to explore the changes imposed by the dynamic electron correlation on the location, topology, and electronic structure of the CI originally located at the CASSCF level. The changes in energy profile along the BLA path can be interpreted in terms of a valence-bond diagram reporting the energies of the  $\psi_{CT}$  and  $\psi_{DIR}$  configurations/diabatic states along the path. The transition states are located, roughly, at the minima of these two diabatic states. At the CASSCF level, the energies of the  $\psi_{CT}$  at  $TS_{CT}$  and  $\psi_{DIR}$  at  $TS_{DIR}$  (see dashed curves in Figure 2C) are relatively close (see double arrow in Figure 2C). As a consequence, the CI point has a “peaked” shape, and both transition states reside on  $S_0$ . However, at the MRCISD+Q level, the  $\psi_{CT}$  state is largely stabilized with respect to  $\psi_{DIR}$  (see double arrow in Figure 2D). Consequently, the CI moves to larger BLA values and changes shape, becoming a sloped or intermediate CI.<sup>14</sup> In this situation,  $TS_{DIR}$  disappears from  $S_0$  and becomes an  $S_1$  minimum along the BLA coordinate.

At the CI, the molecular modes  $X_1$  and  $X_2$  correspond to the gradient difference and derivative coupling and define the so-called branching plane.<sup>14</sup> As shown in Figure 3A, it is apparent that the  $X_1$  and  $X_2$  modes are primarily related to the RC and BLA coordinates, respectively.<sup>42</sup> With this information, we compute a set of branching plane structures located along a small circle centered at the CI. In Figure 3B, we show the CASSCF/6-31G\*  $S_0$  energy profile along the circle and the

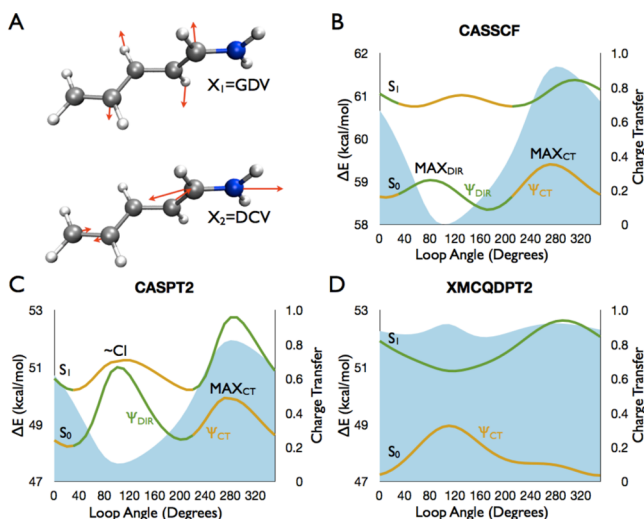


**Figure 3.** The CASSCF/6-31G\* branching plane of PSB3. (A) Modes corresponding to the gradient difference vector (GDV) and derivative coupling vector (DCV). GDV corresponds to the RC (isomerization/pyramidalization) mode, while DCV represents a BLA mode. (B, C, and D) The CASSCF, CASPT2, and XMCQDPT2  $S_0$  and  $S_1$  energies (solid lines) and charge transfer character (blue area) along a circle (radius = 0.002 Å, 1 step every 10°) centered on the CI structure intercepted along the BLA coordinate. The energies are relative to *cis*-PSB3. The charge transfer character is described by the value of the sum of the Mulliken charges on the allyl fragment (C5H<sub>2</sub>–C4H–C3H–). Brown regions correspond to regions dominated by a charge transfer wave function, while green regions are predominantly covalent.

corresponding charge distribution (to monitor the wave function character). The plot shows two energy maxima ( $MAX_{DIR}$  and  $MAX_{CT}$ ) at ca. 80° and 270°. These correspond to ridges developing toward  $TS_{DIR}$  and  $TS_{CT}$ .  $MAX_{DIR}$  and  $MAX_{CT}$  are roughly oriented in the direction of  $X_2$  and feature a covalent and charge-transfer character, respectively, consistent with the results of Figure 2. The two minima along the profile of Figure 3B (ca. 10° and 180°) are associated with the *cis*-PSB3 and *trans*-PSB3 energy valleys (i.e., equilibrium structures) and are located along  $X_1$ . In Figure 3C and D, we show that the changes imposed by the dynamic electron correlation on the relative stability of  $S_0$  and  $S_1$  energy are consistent with the results of Figure 2. For instance, at the XMCQDPT2 level it is clear that the CI point has shifted so much that it is not inside the loop anymore and the wave function character is exclusively dominated by  $\psi_{CT}$ . Clearly, the CASPT2 represents an intermediate case where the CI point is now located on the loop itself at ca. 110°.

**MEP<sub>CT</sub> Path.** The energy profiles along  $MEP_{CT}$  are shown in Figure 4A. Of course, the order of the energies at  $TS_{CT}$  reflects the order of the energies seen in Figure 2. Consistently, the barrier at the  $TS_{CT}$  is lowest at the QD-NEVPT2 level, followed by XMCQDPT2, CASPT2, CASPT2(IPEA=0.25), and MS-CASPT2(IPEA=0.25), all giving barrier heights similar to the one computed at the MRCISD+Q level. In all cases, the dynamic electron correlation decreases the activation energy along  $MEP_{CT}$ . The MEP shows substantially equivalent energy changes when moving toward *cis*-PSB3 and *trans*-PSB3. Thus, starting at  $TS_{CT}$ , one sees that the CASSCF/6-31G\* electronic structure changes from a pure charge-transfer to one where the covalent character eventually becomes predominant. This evolution can be monitored by plotting the charge-distribution along the  $MEP_{CT}$  profile (Figure 4B).  $TS_{CT}$  has nearly 90% of its positive charge on the allyl moiety. However, as the molecule moves away from  $TS_{CT}$ , the system quickly loses its charge-transfer character.

The charge transfer profiles for multireference methods are also plotted in Figure 4B. We find that, in general, methods that stabilize the  $\psi_{CT}$  wave function with respect to  $\psi_{DIR}$  have a more extended charge transfer region along  $MEP_{CT}$ . CASPT2 has a very limited effect on the charge transfer profile because (as shown in Figure 2A) it stabilizes the  $\psi_{CT}$  and  $\psi_{DIR}$  energy profiles to an almost equal extent. The fact that the CASPT2 charge transfer profile is slightly reduced compared to CASSCF may be due to the missing contribution from the relaxation of the orbital and CI-coefficients in CASPT2, which is expected to slightly increase ionic character.

At the MS-CASPT2 level, on the other hand, there is a large extension of the MS-CASPT2 charge transfer region as seen in Figure 4B. This is due to an overestimation of off-diagonal matrix elements of the effective Hamiltonian and thus to overestimation of zero-order state mixing.<sup>20</sup> This is also reflected in the MS-CASPT2 energy profile (Figure 4A) where there is a large stabilization of  $S_0$  (and destabilization of  $S_1$  as shown in the SI) as the molecule moves away from  $TS_{CT}$ , resulting in an irregular energy profile.

The rest of the methods (XMCQDPT2, QD-NEVPT2, and MRCISD) all lead to an extension of the charge transfer region compared to CASSCF. XMCQDPT2 and MRCISD have similar charge transfer profiles because they both have a similar relative stability of the  $\psi_{CT}$  and  $\psi_{DIR}$  wave functions (as indicated by the fact that they display a similar position of the CI along the BLA coordinate; see Figure 2A). QD-NEVPT2



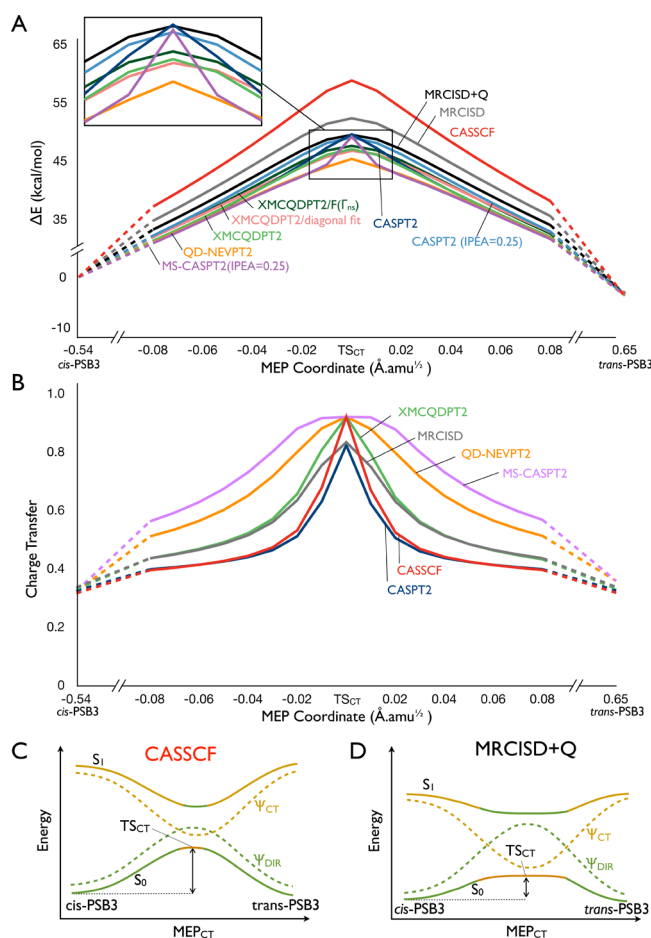


**Figure 4.** Energy profiles along the  $\text{MEP}_{\text{CT}}$  coordinate. (A) The  $S_0$  energies computed using two-root SA-CASSCF (red), MRCISD (gray), MRCISD+Q (black), CASPT2 (dark blue), CASPT2 (IPEA=0.25) (blue), MS-CASPT2 (IPEA=0.25) (violet), QD-NEVPT2 (orange), XMCQDPT2 (green), XMCQDPT2 with a diagonal fit (pink), and XMCQDPT2/ $F(\Gamma_{\text{ms}})$  (dark green). The energies are relative to the reactant (*cis*-PSB3, point  $-0.54$ ). The inset shows an expansion of the region from MEP coordinate  $-0.02$  to  $0.02$ . (B) The charge transfer character along  $\text{MEP}_{\text{CT}}$  for CASSCF, MRCISD, XMCQDPT2, CASPT2, MS-CASPT2, and QD-NEVPT2. (C and D) Schematic valence bond-like state mixing diagrams for the  $S_0$  and  $S_1$  energy profiles along  $\text{MEP}_{\text{CT}}$  at the CASSCF and MRCISD+Q levels of theory, respectively. The diabatic states are represented with dashed lines. Mixing of the diabatic states produces the adiabatic states represented with solid lines. Brown regions correspond to regions dominated by a charge transfer wave function, while green regions are predominantly covalent.

has a more extended charge transfer region due to its over-stabilization of  $\psi_{\text{CT}}$  with respect to  $\psi_{\text{DIR}}$ . MRCISD+Q would be expected to have a charge transfer profile in between that of MRCISD and QD-NEVPT2 since it stabilizes  $\psi_{\text{CT}}$  with respect to  $\psi_{\text{DIR}}$  more than MRCISD does but not to the same extent as QD-NEVPT2.

Again, these results can be interpreted in terms of a valence-bond state mixing diagram and focusing on the  $\text{MEP}_{\text{CT}}$  path. In Figure 4C, we show schematic energy profiles reporting the change in energy of the  $\psi_{\text{CT}}$  and  $\psi_{\text{DIR}}$  configurations/diabatic states along the path. The adiabatic  $S_0$  and  $S_1$  energy profiles originate from the mixing of the two configurations that also determine the variation in electronic structure (charge-transfer vs covalent-diradical) in different regions of the energy profile.

At the CASSCF level, the two states are rather distant in energy and effectively cross only in a limited region corresponding to the vicinity of the  $\text{TS}_{\text{CT}}$  structure. As a consequence, upon relaxation toward *cis*-PSB3 and *trans*-PSB3, the  $S_0$  electronic structure rapidly changes character and becomes dominated by a covalent-diradical electron distribution. This explains why the CASSCF charge-transfer region of the  $S_0$  energy potential energy surface has a limited extension, as shown in Figure 4B and schematically illustrated in Figure 4C. The inclusion of dynamic electron correlation energy leads to the changes shown in Figure 4D as it stabilizes the  $\psi_{\text{CT}}$  state with respect to the  $\psi_{\text{DIR}}$  state. As a consequence, the  $\psi_{\text{CT}}$  energy profile is shifted to lower energies, and  $\psi_{\text{CT}}$  and  $\psi_{\text{DIR}}$  intersect along a larger region. Consequently, the energy of the  $\text{TS}_{\text{CT}}$  is lowered with respect to *cis*-PSB3 and *trans*-PSB3 (the  $\text{MEP}_{\text{CT}}$  path becomes the energetically dominating  $S_0$  path), and the charge-transfer region dominates a larger and flatter region of the  $S_0$  potential energy surface around the  $\text{TS}_{\text{CT}}$  point (see Figure 4D).

**$\text{MEP}_{\text{DIR}}$  Path.** The energy and charge transfer profiles along  $\text{MEP}_{\text{DIR}}$  are shown in Figure 5A and B, respectively. The effect of the electron dynamic correlation on the CASSCF/6-31G\* energy profile is similar to the one found for  $\text{MEP}_{\text{CT}}$ . The barriers (with respect to *cis*-PSB3) are always decreased with respect to the CASSCF level, but the magnitude of this change is substantially smaller than that observed in  $\text{MEP}_{\text{CT}}$ . In the case of MS-CASPT2 (IPEA=0.25), we see the same artifact as in  $\text{MEP}_{\text{CT}}$ , displaying an extremely rapid decrease in energy when moving away from the transition state. The other methods all give a much smoother profile. There is a strong agreement between the XMCQDPT2, CASPT2, and QD-NEVPT2 in their energy profile along  $\text{MEP}_{\text{DIR}}$ .

The charge transfer profile along  $\text{MEP}_{\text{DIR}}$  shows that CASSCF has the widest diradical region, while the MRPT2 methods and MRCISD reduce the size of the diradical region. In general, we find that methods that extend the charge transfer profile along  $\text{MEP}_{\text{CT}}$  (Figure 4B) tend to reduce the diradical region along  $\text{MEP}_{\text{DIR}}$  (Figure 5B) because  $\psi_{\text{DIR}}$  gets destabilized relative to  $\psi_{\text{CT}}$ . Consistently, note that MS-CASPT2, which has the widest  $\psi_{\text{CT}}$  region along  $\text{MEP}_{\text{CT}}$ , displays the narrowest diradical region along  $\text{MEP}_{\text{DIR}}$  (and interestingly, gains some  $\psi_{\text{CT}}$  character before returning to the covalent region near the *cis* and *trans* equilibrium geometries). Moreover, since the  $\text{MEP}_{\text{DIR}}$  path intersects with the BLA path at a BLA coordinate of around  $0.025 \text{ \AA}$ , methods that result in a CI with a higher BLA than  $0.025 \text{ \AA}$  (i.e., a sloped or intermediate CI) would still have an  $S_0$  state with charge transfer rather than diradical character at the  $\text{TS}_{\text{DIR}}$  geometry. Effectively, this moves the corresponding  $\text{TS}_{\text{DIR}}$  minimum along the BLA coordinate from the  $S_0$  state to the  $S_1$  state. These same methods would display an inverted charge transfer profile along  $\text{MEP}_{\text{DIR}}$  with respect to the other methods (see, for example, the QD-NEVPT2 charge transfer profile in Figure 5B). This is expected to be the case for all the multireference methods shown in Figure 2B.

Again, the charge transfer profiles along  $\text{MEP}_{\text{DIR}}$  can be explained when comparing the valence bond diagrams in Figure 5C and D. At the CASSCF level, the diabatic states do not cross, and the diabatic and adiabatic states have similar profiles. Stabilization of the  $\psi_{\text{CT}}$  diabatic state with MRCISD+Q causes the  $\psi_{\text{CT}}$  state to become lower in energy than the  $\psi_{\text{DIR}}$  state along part of the  $\text{MEP}_{\text{DIR}}$  path (with the two states being nearly degenerate at  $\text{TS}_{\text{DIR}}$ ).

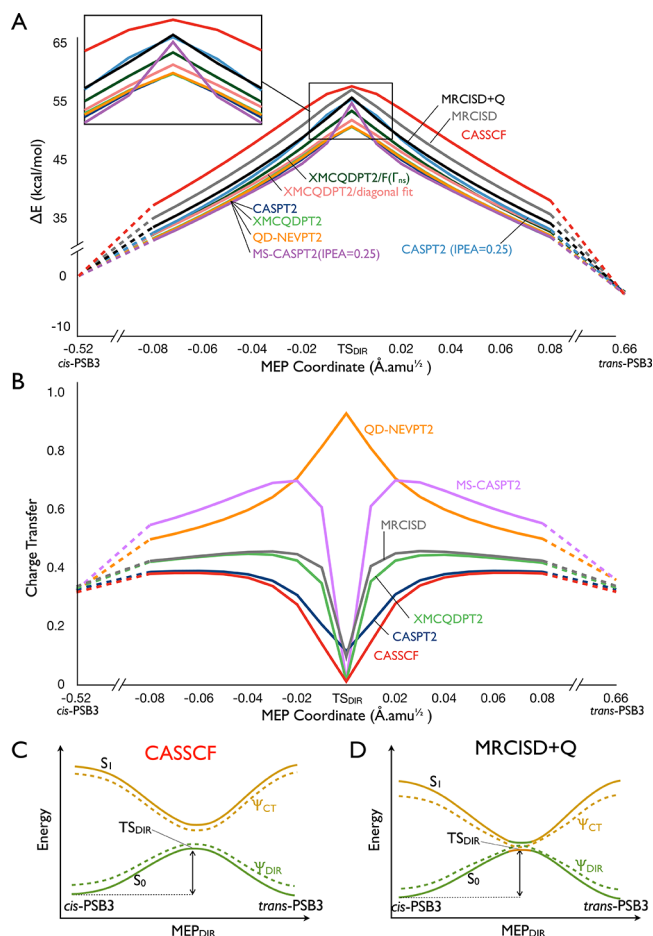
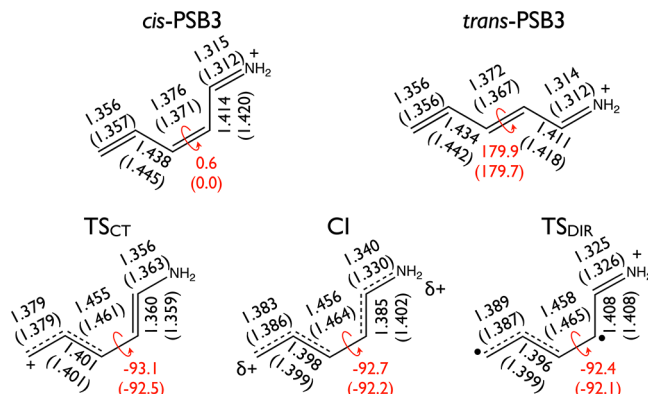


**Figure 5.** Energy profiles along the  $\text{MEP}_{\text{DIR}}$  coordinate. (A) The  $S_0$  energies computed using two-root SA-CASSCF (red), MRCISD (gray), MRCISD+Q (black), CASPT2 (dark blue), CASPT2-IPEA=0.25 (blue), MS-CASPT2(IPEA=0.25) (violet), QD-NEVPT2 (orange), XMCQDPT2 (green), XMCQDPT2 with a diagonal fit (pink), and XMCQDPT2/ $F(\Gamma_{\text{ns}})$  (dark green). The energies are shown relative to the reactant (*cis*-PSB3, point  $-0.52$ ). The inset shows an expansion of the region from MEP coordinate  $-0.02$  to  $0.02$ . (B) The charge transfer character along  $\text{MEP}_{\text{DIR}}$  for CASSCF, MRCISD, XMCQDPT2, CASPT2, MS-CASPT2, and QD-NEVPT2. (C and D) Schematic valence bond-like state mixing diagrams for the  $S_0$  and  $S_1$  energy profiles along  $\text{MEP}_{\text{DIR}}$  at the CASSCF and MRCISD+Q levels of theory, respectively. The diabatic states are represented with dashed lines. Mixing of the diabatic states produces the adiabatic states represented with solid lines. Brown regions correspond to regions dominated by a charge transfer wave function while green regions are predominantly covalent.

**Effect of the Geometry Optimization.** The analysis above has consistently been based on structures located using CASSCF/6-31G\* analytical gradients. In this section, we will investigate the effect of reoptimizing the geometries of the four stationary points (*cis*-PSB3, *trans*-PSB3,  $\text{TS}_{\text{CT}}$ , and  $\text{TS}_{\text{DIR}}$ ) at the CASPT2/6-31G\* and XMCQDPT2/6-31G\* levels using a two-root SA-CASSCF wave function as the zeroth-order wave function and numerical gradients. The high computational cost prevents a study at the MRCISD+Q level due to the size of our reference space used. While the CASSCF and MRPT2 structures display very similar dihedral and bending angles, there are some differences between bond lengths, consistent with earlier studies.<sup>2,6</sup> The structures optimized at the MRPT2 level of theory are shown in Scheme 3. While CASSCF tends to

**Scheme 3.** The Structures of *cis*-PSB3, *trans*-PSB3,  $\text{TS}_{\text{CT}}$ , and  $\text{TS}_{\text{DIR}}$  All Optimized at the MRPT2 Level of Theory, As Well as the Structure of the CI Intercepted by the BLA Scans in Figure 6A<sup>a</sup>



<sup>a</sup>Bond lengths, as well as the central isomerization angle, are labeled for both the CASPT2 and XMCQDPT2 levels of theory (XMCQDPT2 in parentheses).

give a larger BLA value,<sup>2,6</sup> this change is limited with the exception of the CI–N bond and (to a smaller extent) the C5–C4 bond (compare Schemes 2 and 3). We plot the CASSCF, CASPT2, and XMCQDPT2 energies (optimized at the respective method) along the BLA coordinate in Figure 6A (CASPT2 displays an artifact near the center of the curve due to its proximity to the CASSCF CI<sup>20,40</sup>). We find that while the position of  $\text{TS}_{\text{CT}}$  along the BLA coordinate is not largely affected,  $\text{TS}_{\text{DIR}}$  displays the largest variation and moves to lower BLA values with both CASPT2 and XMCQDPT2. However, the position of the CI is relatively unaffected by the MRPT2 optimization. We find, consistently with the results of Figure 2A, that the CASPT2 CI is close to the CASSCF CI but has a slightly higher BLA, while the XMCQDPT2 CI is over  $0.01$  Å higher along the BLA coordinate. In spite of the geometrical differences observed for  $\text{TS}_{\text{DIR}}$ , there is a limited change in the relative energies with respect to the *cis*-PSB3 geometry (see Table 1, where we compare MRPT2 relative energies for CASSCF and MRPT2 geometries).  $\text{TS}_{\text{DIR}}$  is stabilized with respect to  $\text{TS}_{\text{CT}}$  after CASPT2 and XMCQDPT2 optimizations, but in both cases the effect is such that  $\text{TS}_{\text{CT}}$  remains the lowest in energy (with the XMCQDPT2  $\text{TS}_{\text{CT}}$  lower in energy than the CASPT2  $\text{TS}_{\text{CT}}$ , consistently with the results in Figure 2A). In Figure 6B and C, we display the energy profiles along  $\text{MEP}_{\text{CT}}$  and  $\text{MEP}_{\text{DIR}}$  coordinates optimized starting from the  $\text{TS}_{\text{CT}}$  and  $\text{TS}_{\text{DIR}}$  structures at the corresponding MRPT2 levels (i.e., starting from the MRPT2-optimized transition states, the path points were generated at the respective MRPT2 level of theory as well). The results are compared with the MRPT2//CASSCF  $\text{MEP}_{\text{CT}}$  and  $\text{MEP}_{\text{DIR}}$  in the same figure. We find that the minimum energy path geometries generated with the MRPT2//MRPT2 methods are similar to the ones generated at the MRPT2//CASSCF level. Overall, the results of Figure 6 and Table 1 indicate that the MRPT2//MRPT2  $S_0$  potential energy surface near the CI is very similar to the MRPT2//CASSCF one, except that the valleys corresponding to the  $\text{MEP}_{\text{CT}}$  and  $\text{MEP}_{\text{DIR}}$  paths must be geometrically closer to each other since the distance between  $\text{TS}_{\text{CT}}$  and  $\text{TS}_{\text{DIR}}$  along the BLA coordinate is closer at the MRPT2 levels with respect to the CASSCF level.

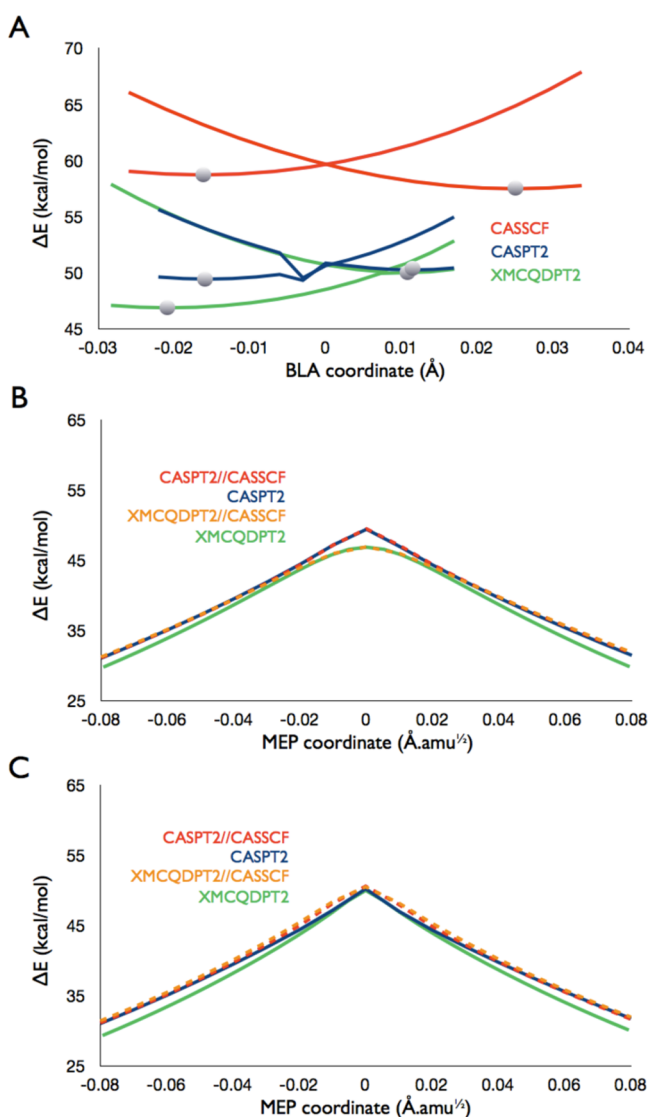


**Figure 6.** (A) The CASSCF, CASPT2, and XMCQDPT2 energies plotted along a BLA coordinate. The interpolated structures were generated from  $TS_{CT}$  and  $TS_{DIR}$  optimized at the respective level of theory. The energies are relative to *cis*-PSB3 optimized at the same level of theory. The positions of the optimized transition states along the BLA coordinate are marked with gray circles. CASPT2 displays an artifact near the center of the curve due to its proximity to the CASSCF CI. (See also text; B and C) The MRPT2 energies along the  $MEP_{CT}$  and  $MEP_{DIR}$  paths computed using MRPT2 numerical gradients (solid lines) and their energies along the same path computed at the CASSCF level of theory (dashed lines).

**Table 1. The Relative MRPT2 Energies of *trans*-PSB3,  $TS_{CT}$ , and  $TS_{DIR}$  Computed at the MRPT2 and CASSCF Optimized Geometries<sup>a</sup>**

energy	CASPT2	CASPT2	XMCQDPT2	XMCQDPT2
geometry	CASSCF	CASPT2	CASSCF	XMCQDPT2
<i>trans</i> -PSB3 (kcal/mol)	-3.1	-3.1	-2.8	-2.8
$TS_{CT}$ (kcal/mol)	49.3	49.4	46.9	46.9
$TS_{DIR}$ (kcal/mol)	50.6	50.3	50.5	50.0

<sup>a</sup>The single point energy calculations and optimizations were performed with the 6-31G\* basis set. The energies are relative to *cis*-PSB3.

**Remarks on the CASPT2//CASSCF/6-31G\* Level.** The CASPT2//CASSCF/6-31G\* protocol has been widely used for evaluating vertical and 0–0 excitation energies as well as ground and excited state reaction barriers. For instance, this methodology has been used in quantum-mechanics/molecular-mechanics computation to investigate the spectroscopy of different proteins yielding absorption maxima with errors of a few kcal/mol with respect to experimentally determined values.<sup>10,43–47</sup> Here, we use the PSB3 results to assess the validity of this protocol by comparing CASPT2//CASSCF/6-31G\* relative energies with the corresponding quantities computed at the CASPT2(IPEA=0.25)/ANO-VDZP and CASPT2(IPEA=0.25)/ANO-VTZP levels using the CASPT2/6-31G\* geometry.

The results in Table 2 indicate that the success of the CASPT2//CASSCF/6-31G\* protocol in predicting vertical excitation energies can be attributed to a cancellation of errors. Larger basis sets would red-shift the computed excitation energy. We also find that optimizing the ground state reactant at the CASPT2 level rather than the CASSCF level before evaluating the excitation energy also red-shifts the absorption, consistent with a recent study.<sup>48</sup> On the other hand, the more accurate CASPT2(IPEA=0.25) level (i.e., the use of the IPEA shift), in all cases, leads to blue-shifting. The data in Table 2 show that, for PSB3, the red-shifting and blue-shifting effects counterbalance each other when using CASPT2(IPEA=0.25) and large basis sets such as ANO-VTZP and more so when also using the CASPT2 optimized geometry. This is consistent with findings in a previous study on adenine,<sup>49</sup> and with data presented in ref 6. As a result, we find that the computed CASPT2//CASSCF/6-31G\* value is close to experimentally determined absorption maxima available for a PSB3 derivative<sup>50</sup> which, however, have been recorded in methanol and dichloromethane.

The cancellation effects do not appear to operate when evaluating the reaction barriers or the relative stability of  $TS_{CT}$  and  $TS_{DIR}$ . In this case, it appears to be more accurate to use the CASPT2(IPEA=0.25)//CASSCF/6-31G\* level. In fact, this level produces barriers and stabilities close to the ones computed at the CASPT2(IPEA=0.25)/ANO-VTZP level using the CASPT2/6-31G\* optimized geometry. The failure of the cancellation effect in this case can be understood by considering the nature of the wave function characterizing  $S_0$  and  $S_1$  at *cis*-PSB3 and of the wave functions characterizing  $TS_{DIR}$  and  $TS_{CT}$ . A simple analysis reveals that the  $S_1$  wave function of *cis*-PSB3 and *trans*-PSB3, which is dominated by a charge-transfer configuration, has a certain percentage of diradical character with respect to the closed-shell character of the ground state. Since the IPEA shift is known to increase the energy of open-shell states,<sup>26</sup> it is evident that the CASPT2(IPEA=0.25) level blue-shifts the absorption (opposite of the basis set effect that stabilizes charge-transfer states with respect to the ground state). In contrast, when computing the relative transition state stability, the situation is inverted. In fact, in this case,  $TS_{DIR}$  has an almost purely diradical character state, while  $TS_{CT}$  is closed-shell such that the IPEA shift and basis set effect go in the same direction. Therefore, we find that the IPEA shift increases the  $TS_{DIR}$  barrier, while the improvement of the basis set primarily stabilizes the  $TS_{CT}$  barrier.

## CONCLUSIONS AND PERSPECTIVES

Our computations demonstrate that the low-lying cross sections of the  $S_0$  CASSCF potential energy surface of PSB3

**Table 2.** The Effect of Using CASPT2(IPEA=0.25), Expanding the Basis Set, and Optimizing the Structures at the CASPT2 Level on the Vertical Excitation Energies at the *cis*-PSB3 and *trans*-PSB3 Geometries, the Activation Barriers via TS<sub>CT</sub> and TS<sub>DIR</sub>, and on the Relative Energies of S<sub>0</sub> *cis*-PSB3 and *trans*-PSB3<sup>a</sup>

Energy	CASPT2(IPEA=0) (6-31G*)	CASPT2(IPEA=0.25) (6-31G*)	CASPT2(IPEA=0.25) (ANO-L-VDZP)	CASPT2(IPEA=0.25) (ANO-L-VTZP)	CASPT2(IPEA=0.25) (ANO-L-VTZP)	CASPT2(IPEA=0.25) (ANO-L-VTZP)
Geometry	CASSCF (6-31G*)	CASSCF (6-31G*)	CASSCF (6-31G*)	CASSCF (6-31G*)	CASPT2(6-31G*)	CASPT2(6-31G*)
<i>cis</i> -PSB3 S <sub>0</sub> -S <sub>1</sub> excitation energy (kcal/mol)	92.0	98.2	95.1	94.1	93.2	92.3 (92.2)*
<i>trans</i> -PSB3 S <sub>0</sub> -S <sub>1</sub> excitation energy (kcal/mol)	94.4	100.9	98.6	97.6	97.1	96.2
<i>trans</i> -PSB3 S <sub>0</sub> energy relative to <i>cis</i> -PSB3 (kcal/mol)	-3.1	-3.1	-2.9	-2.8	-2.9	-2.8
TS <sub>CT</sub> S <sub>0</sub> energy relative to <i>cis</i> -PSB3 (kcal/mol)	49.3	48.9	47.6	48.0	47.6	48.0
TS <sub>DIR</sub> S <sub>0</sub> energy relative to <i>cis</i> -PSB3(kcal/mol)	50.6	55.2	54.6	56.3	54.4	56.2

<sup>a</sup>Highlighted cells correspond to the methods that best reproduce the energies obtained at the superior CASPT2(IPEA=0.25)/ANO-L-VTZP//CASPT2/6-31G\* level of theory (right column) but at a much lower computational cost. An asterisk (\*) indicates that the value in parentheses is an experimentally determined excitation energy of a PSB3 derivative from ref 50. Note however that this value was measured in methanol and dichloromethane, and corresponds to the absorption maximum, and therefore only gives us a rough estimate of the vertical absorption value of gas-phase PSB3.

investigated in this work are qualitatively different when computed with methodologies accounting for dynamic electron correlation. In general, both MRCISD+Q and all MRPT2 implementations point to a large stabilization of the region dominated by the charge-transfer configuration ( $\psi_{CT}$ ) with respect to the region dominated by a covalent-diradical structure ( $\psi_{DIR}$ ). The stabilization of the charge-transfer region is also reflected by its extension along the RC coordinate. A similar effect is seen when one augments the basis set with polarization and diffuse functions, which allows for a better description of the charge distribution of the charge transfer configuration.

The rather dramatic change in shape of the CASSCF energy surface (Figure 7A) with respect to electron correlated surfaces

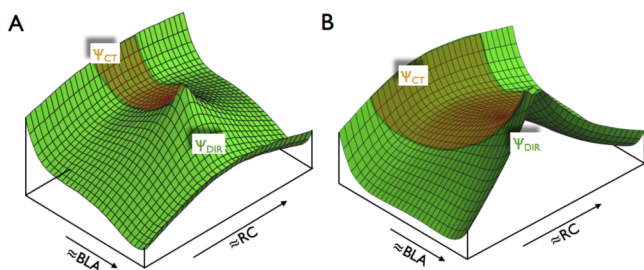


**Figure 7.** (A) Schematic shape of the S<sub>0</sub> CASSCF potential energy surface consistent with the results of our computations. (B) The same schematic representations based on the results of MRCISD+Q computations.

(Figure 7B) suggests that the relaxation dynamics occurring immediately after the decay at the CI could be qualitatively different in these two situations. The peaked CI of the CASSCF energy surface would probably favor a “ballistic” decay where the majority of the population would hop during the first approach to the CI region. The same surface suggests that after decay the population will mainly be collected in a covalent/diradical region favoring reconstitution of the central double bond. In contrast, the MRCISD+Q energy surface featuring a sloped-intermediate CI would probably drive a less straightforward decay process. As a consequence, while our study indicates that CASSCF may still be used to study the mechanism of the photochemical process in question (e.g. CASSCF minima, transition states, CI and MEPs provide correct information on the character of the reaction coordinates

driving the isomerization of PSB3), caution must be exercised when drawing quantitative and statistical conclusions from a set of semiclassical trajectory calculations,<sup>15,51–53</sup> especially in terms of reaction time scales and branching of the excited state population after the decay. One remarkable feature is the flattening and widening of the charge transfer region, which suggests that a larger number of trajectories will be collected in this region, thus producing longer-lived transient species with the features of an intramolecular twisted charge-transfer state. In principle, similar changes may also have an impact on our understanding of the dynamics associated with the photoisomerization of visual pigments. The PSB5 model incorporating five conjugating double bonds (and therefore closer to rPSB) has the TS<sub>DIR</sub> and TS<sub>CT</sub> transition states separated by 0.7 kcal/mol on the CASSCF energy surface.<sup>8,9</sup> In this situation, it is likely that the charge-transfer state becomes, as indicated by our shorter model, stabilized by the dynamic electron correlation yielding similar dramatic effects on the ground state relaxation dynamics even when embedded in a protein cavity. Of course, as previously reported,<sup>54–57</sup> the protein environment and the solvent may have important additional effects on the relative stability of the charge transfer and diradical/covalent regions of the S<sub>0</sub> potential energy surface. This has recently been shown for bovine rhodopsin via CASPT2//CASSCF/MM computations.<sup>54</sup> More studies in this direction are needed to fully evaluate the magnitude of these effects.

## ■ ASSOCIATED CONTENT

### 📄 Supporting Information

Supporting text and figures providing additional information about NEVPT2, XMCQDPT2, and MRCISD methods. A discussion and figures regarding the artifacts in CASPT2 and MS-CASPT2, the effect of expanding the basis set, the active space, and the number of roots in state averaged computations. Cartesian coordinates of CASSCF optimized structures. This material is available free of charge via the Internet at <http://pubs.acs.org/>.

## ■ AUTHOR INFORMATION

### Corresponding Author

\*E-mail: molivuc@bgnet.bgsu.edu.

## Present Address

<sup>#</sup>Max Planck Institute for Bioinorganic Chemistry, Mülheim, Stiftstraße 34-36, 45470 Mülheim, Germany.

## Notes

The authors declare no competing financial interest.

## ACKNOWLEDGMENTS

This work was supported by the Bowling Green State University. M.O. is grateful to the Center for Photochemical Sciences of Bowling Green State University for start-up funds. R.L. recognizes funding from the Swedish Research Council (VR). C.A. has been financed by the Italian MIUR through its PRIN 2009 funds. We are grateful to the Ohio Supercomputer Center, NSF-TeraGrid (XSEDE), and CINECA for granted computer time.

## REFERENCES

- (1) Garavelli, M.; Bernardi, F.; Robb, M. A.; Olivucci, M. *J. Mol. Struct.: THEOCHEM* **1999**, *463*, 59–64.
- (2) Page, C. S.; Olivucci, M. *J. Comput. Chem.* **2003**, *24*, 298–309.
- (3) Sinicropi, A.; Migani, A.; De Vico, L.; Olivucci, M. *Photochem. Photobiol. Sci.* **2003**, *2*, 1250–5.
- (4) Fantacci, S.; Migani, A.; Olivucci, M. *J. Phys. Chem. A* **2004**, *108*, 1208–1213.
- (5) Barbatti, M.; Ruckebauer, M.; Szymczak, J. J.; Aquino, A. J.; Lischka, H. *J. Phys. Chem. Chem. Phys.* **2008**, *10*, 482–94.
- (6) Valsson, O.; Filippi, C. *J. Chem. Theory Comput.* **2010**, *6*, 1275–1292.
- (7) Mori, T.; Nakano, K.; Kato, S. *J. Chem. Phys.* **2010**, *133*, 064107.
- (8) De Vico, L.; Page, C. S.; Garavelli, M.; Bernardi, F.; Basosi, R.; Olivucci, M. *J. Am. Chem. Soc.* **2002**, *124*, 4124–34.
- (9) De Vico, L.; Garavelli, M.; Bernardi, F.; Olivucci, M. *J. Am. Chem. Soc.* **2005**, *127*, 2433–42.
- (10) Andrúniów, T.; Ferré, N.; Olivucci, M. *Proc. Natl. Acad. Sci. U. S. A.* **2004**, *101*, 17908–13.
- (11) Garavelli, M.; Celani, P.; Bernardi, F.; Robb, M. A.; Olivucci, M. *J. Am. Chem. Soc.* **1997**, *119*, 6891–6901.
- (12) Migani, A.; Robb, M. A.; Olivucci, M. *J. Am. Chem. Soc.* **2003**, *125*, 2804–2808.
- (13) Frutos, L. M.; Andrúniów, T.; Santoro, F.; Ferré, N.; Olivucci, M. *Proc. Natl. Acad. Sci. U. S. A.* **2007**, *104*, 7764–9.
- (14) Atchity, G. J.; Xantheas, S. S.; Ruedenberg, K. *J. Chem. Phys.* **1991**, *95*, 1862.
- (15) Schapiro, I.; Ryazantsev, M. N.; Frutos, L. M.; Ferré, N.; Lindh, R.; Olivucci, M. *J. Am. Chem. Soc.* **2011**, *133*, 3354–64.
- (16) González, L.; Escudero, D.; Serrano-Andrés, L. *Chem. Phys. Chem.* **2012**, *13*, 28–51.
- (17) Borden, W. T.; Davidson, E. R. *Acc. Chem. Res.* **1996**, *29*, 67–75.
- (18) Andersson, K.; Malmqvist, P.; Roos, B. O. *J. Chem. Phys.* **1992**, *96*, 1218.
- (19) Finley, J.; Malmqvist, P.; Roos, B. O.; Serrano-Andrés, L. *Chem. Phys. Lett.* **1998**, *288*, 299–306.
- (20) Granovsky, A. A. *J. Chem. Phys.* **2011**, *134*, 214113.
- (21) Angeli, C.; Cimraglia, R.; Evangelisti, S.; Leininger, T.; Malrieu, J. P. *J. Chem. Phys.* **2001**, *114*, 10252.
- (22) Angeli, C.; Borini, S.; Cestari, M.; Cimraglia, R. *J. Chem. Phys.* **2004**, *121*, 4043–9.
- (23) Angeli, C.; Pastore, M.; Cimraglia, R. *Theor. Chem. Acc.* **2007**, *117*, 743–754.
- (24) Aquilante, F.; De Vico, L.; Ferré, N.; Ghigo, G.; Malmqvist, P. A.; Neogrády, P.; Pedersen, T. B.; Pitonák, M.; Reiher, M.; Roos, B. O.; Serrano-Andrés, L.; Urban, M.; Velyazov, V.; Lindh, R. *J. Comput. Chem.* **2010**, *31*, 224–47.
- (25) Frisch, M. J.; Trucks, G. W.; Schlegel, H. B.; Scuseria, G. E.; Robb, M. A.; Cheeseman, J. R.; Montgomery Jr, J. A.; Vreven, T.; Kudin, K. N.; Burant, J. C. *Gaussian 03, C.02*; Gaussian Inc.: Wallingford, CT, 2004.
- (26) Ghigo, G.; Roos, B. O.; Malmqvist, P. *Chem. Phys. Lett.* **2004**, *396*, 142–149.
- (27) Kepenekian, M.; Robert, V.; Le Guennic, B. *J. Chem. Phys.* **2009**, *131*, 114702–114709.
- (28) Granovsky, A. A. *Firefly*, version 7.1.G. <http://classic.chem.msu.su/gran/firefly/index.html> (accessed September 2012).
- (29) Werner, H. J.; Knowles, P. J. *J. Chem. Phys.* **1988**, *89*, 5803.
- (30) Werner, H. J.; Knowles, P. J.; Knizia, G.; Manby, F. R.; Schütz, M.; Celani, P.; Korona, T.; Lindh, R.; Mitrushenkov, A.; Rauhut, G.; Shamasundar, K. R.; Adler, T. B.; Amos, R. D.; Bernhardsson, A.; Berning, A.; Cooper, D. L.; Deegan, M. J. O.; Dobbyn, A. J.; Eckert, F.; Goll, E.; Hampel, C.; Hesselmann, A.; Hetzer, G.; Hrenar, T.; Jansen, G.; Köppl, C.; Liu, Y.; Lloyd, A. W.; Mata, R. A.; May, A. J.; McNicholas, S. J.; Meyer, W.; Mura, M. E.; Nicklass, A.; O'Neill, D. P.; Palmieri, P.; Pflüger, K.; Pitzer, R.; Reiher, M.; Shiozaki, T.; Stoll, H.; Stone, A. J.; Tarroni, R.; Thorsteinsson, T.; Wang, M.; Wolf, A. *MOLPRO*, version 2010.1; Cardiff University: Cardiff, U. K.; Universität Stuttgart: Stuttgart, Germany, 2010.
- (31) Lischka, H.; Shepard, R.; Brown, F. B.; Shavitt, I. *Int. J. Quantum Chem.* **1981**, *20*, 91–100.
- (32) Lischka, H.; Shepard, R.; Pitzer, R. M.; Shavitt, I.; Dallos, M.; Müller, T.; Szalay, P. G.; Seth, M.; Kedziora, G. S.; Yabushita, S. *Phys. Chem. Chem. Phys.* **2001**, *3*, 664–673.
- (33) Lischka, H.; Shepard, R.; Shavitt, I.; Pitzer, R. M.; Dallos, M.; Müller, T.; Szalay, P. G.; Brown, F. B.; Ahlrichs, R.; Boehm, H. J. *COLUMBUS*, release 5.9.1; Institute for Theoretical Chemistry, University of Vienna: Vienna, Austria, 2006.
- (34) Shepard, R.; Shavitt, I.; Pitzer, R. M.; Comeau, D. C.; Pepper, M.; Lischka, H.; Szalay, P. G.; Ahlrichs, R.; Brown, F. B.; Zhao, J. G. *Int. J. Quantum Chem.* **1988**, *34*, 149–165.
- (35) Helgaker, T.; Jensen, H. J. A.; Jørgensen, P.; Olsen, J.; Ruud, K.; Ågren, H.; Andersen, T.; Bak, K. L.; Bakken, V.; and Christiansen, O. *DALTON*, Release 1.0. <http://www.kjemi.uio.no/software/dalton/dalton.html> (accessed September 2012).
- (36) Gonzalez, C.; Schlegel, H. B. *J. Chem. Phys.* **1989**, *90*, 2154.
- (37) Jiang, W.; Wilson, A. K. *J. Chem. Phys.* **2011**, *134*, 034101.
- (38) Angeli, C.; Pastore, M. *J. Chem. Phys.* **2011**, *134*, 184302.
- (39) Werner, H. J.; Kállay, M.; Gauss, J. *J. Chem. Phys.* **2008**, *128*, 034305.
- (40) Malrieu, J. P.; Heully, J. L.; Zaitsevskii, A. *Theor. Chem. Acc.* **1995**, *90*, 167–187.
- (41) Shiozaki, T.; Györfy, W.; Celani, P.; Werner, H. J. *J. Chem. Phys.* **2011**, *135*, 081106.
- (42) Coto, P. B.; Sinicropi, A.; De Vico, L.; Ferré, N.; Olivucci, M. *Mol. Phys.* **2006**, *104*, 983–991.
- (43) Pistolesi, S.; Sinicropi, A.; Pogni, R.; Basosi, R.; Ferré, N.; Olivucci, M. *J. Phys. Chem. B* **2009**, *113*, 16082–90.
- (44) Coto, P. B.; Strambi, A.; Ferré, N.; Olivucci, M. *Proc. Natl. Acad. Sci. U. S. A.* **2006**, *103*, 17154–9.
- (45) Coto, P. B.; Martí, S.; Oliva, M.; Olivucci, M.; Merchan, M.; Andres, J. *J. Phys. Chem. B* **2008**, *112*, 7153–7156.
- (46) Sinicropi, A.; Andrúniów, T.; Ferré, N.; Basosi, R.; Olivucci, M. *J. Am. Chem. Soc.* **2005**, *127*, 11534–5.
- (47) Schapiro, I.; Ryazantsev, M. N.; Ding, W. J.; Huntress, M. M.; Melaccio, F.; Andrúniów, T.; Olivucci, M. *Aust. J. Chem.* **2010**, *63*, 413–429.
- (48) Valsson, O.; Angeli, C.; Filippi, C. *Phys. Chem. Chem. Phys.* **2012**, *14*, 11015–11020.
- (49) Barbatti, M.; Ullrich, S. *Phys. Chem. Chem. Phys.* **2011**, *13*, 15492–500.
- (50) Bissonnette, M.; Le Thanh, H.; Vocelle, D. *Can. J. Chem.* **1984**, *62*, 1459–1464.
- (51) Weingart, O.; Migani, A.; Olivucci, M.; Robb, M. A.; Buss, V.; Hunt, P. *J. Phys. Chem. A* **2004**, *108*, 4685–4693.
- (52) Weingart, O.; Altoè, P.; Stenta, M.; Bottoni, A.; Orlandi, G.; Garavelli, M. *Phys. Chem. Chem. Phys.* **2011**, *13*, 3645–3648.
- (53) Weingart, O.; Garavelli, M. *J. Chem. Phys.* **2012**, *137*, 523–529.
- (54) Gozem, S.; Schapiro, I.; Ferré, N.; Olivucci, M. *Science* **2012**, *337*, 1225–1228.

(55) Munoz-Losa, A.; Martín, M. E.; Fernández Galván, I.; Sánchez, M. L.; Aguilar, M. J. *Chem. Theory Comput.* **2011**, *7*, 4050–4059.

(56) Burghardt, I.; Cederbaum, L. S.; Hynes, J. T. *Faraday Discuss.* **2004**, *127*, 395–411.

(57) Spezia, R.; Burghardt, I.; Hynes, J. T. *Mol. Phys.* **2006**, *104*, 903–914.